A Simulation-Based and Data-Augmented Shear Force Inversion Method for Offshore Platform Connector

Tao Zhang [a], Selda Oterkus [b], Erkan Oterkus [b], Jiajun Hu [a], Xueliang Wang [a], Fang Wang [c]

[a] *Department of Naval Structural, China Ship Scientific Research Center, Wuxi, 214082, China*
[b] *Department of Naval Architecture, Ocean and Marine Engineering, University of Strathclyde, 100 Montrose Street, Glasgow, G4 0LZ, UK*
[c] *Hadal Science and Technology Research Center, Shanghai Ocean University, Shanghai, 201306, China*

Abstract:

This study introduces a Simulation-Based and Data-Augmented method for shear force inversion to address the challenge of directly measuring shear force on connector pins in multi-module floating platforms. Stress sensors are strategically placed in adjacent areas. Extensive Finite Element simulation scenarios lead to the identification of optimal features sensitive to both force magnitude and direction. Subsequently, an Artificial Neural Network (ANN) is developed to distill the simulation data into characteristic sensor responses. Fine-tuning with physical measurements further enhances shear force inversion accuracy. Using simulated and experimental data, the method demonstrates a shear force inversion error below 3.2% and an angular inversion error under 1.4% across test conditions. This methodology provides essential load data for connector safety assessments and crucial guidelines for the assembly of multi-module floating platforms.

Keywords: Offshore Platform; Connector Pin; Shear Force Inversion; ANN; Simulation-Based and Data-Augmented.

1 Introduction

Applications like offshore solar farms, ranches, floating airports, and large floating structures (VLFS) use connectors to manage heavy loads in harsh marine conditions. Fig. 1 depicts an offshore platform consisting of two semi-submersible modules interconnected by rigid, hinged connectors, which enable relative pitching movements between modules and reduce the sectional loads on the structures [1]. The weakest component in the VLFS is identified as the connector pins due to the conversion of relative transverse loads and mooring forces into shear forces. Consequently, assessing the safety and reliability of the VLFS hinges on obtaining the connector shear force. To overcome the challenge posed by the close connection between the pin and the connector, this paper employs a strategic approach by placing stress sensors on adjacent structures to determine the shear forces acting on the connectors accurately.

Fig.1. The connector of two semi-submersible floating platforms

Load inversion techniques have evolved considerably since their inception in the 1970s [2], with applications ranging from infrastructure like bridges [3] and tunnels to vehicles [4], aerospace [5], and marine structures [6,7]. Initially, Vuorio et al. in 1979 applied these techniques to measure shear strain variations on a ship's ribs to infer ice loads [8]. This was followed by Desanghere et al., who 1985 introduced time-domain methods to uncouple dynamic equations for load inversion [9]. By 1996, Callahan et al. had further refined the process by using singular value decomposition to invert dynamic loads and pinpoint their application locations [10]. Recent advancements in load inversion algorithms have been particularly noteworthy in maritime applications [11,12]. Ren et al. have focused on damage prediction for ship hulls [13], while Si et al. introduced a U-shaped measuring beam in 2022 for accurate force simulation on a ship's hull [14]. Meanwhile, Mubarak and Sutrisno have also contributed to the field by investigating methods to ensure ships' structural integrity [15,16].

Complementing these advances, Artificial Intelligence (AI) techniques are increasingly applied in the field of load inversion. For example, Samson et al. achieved a 92% accuracy rate in 2018 using Artificial Neural Networks (ANNs) for static load inversion on aircraft wings [17], and Nan et al. optimized Long Short-Term Memory (LSTM) network structures in 2021 to develop an effective model for ice load inversion [18].

Considering the irregular geometry and varying angles of shear forces on the connector structure, traditional analytical methods require extensive sensor configurations, which can lead to significant cost and noise interference. As a complementary approach, AI-based methods enable strategic sensor placement, effectively capturing the magnitude and direction of shear forces with fewer sensors.

2 Simulation Analysis of the Connector Structure

2.1 Details of the Connector

The offshore platform is assembled from two identical modules through a connector system, which includes two pairs of single-ear and double-ear connectors, all linked via hinge-type pins, as shown in Fig. 2. Internally, the connectors are tightly attached to the main structure of the modules. Both the single-ear and double-ear connectors exhibit axially symmetric designs, incorporating longitudinal frames, transverse frames, ribs, stringers, and cross-bracings to establish an integrated box-shaped framework.

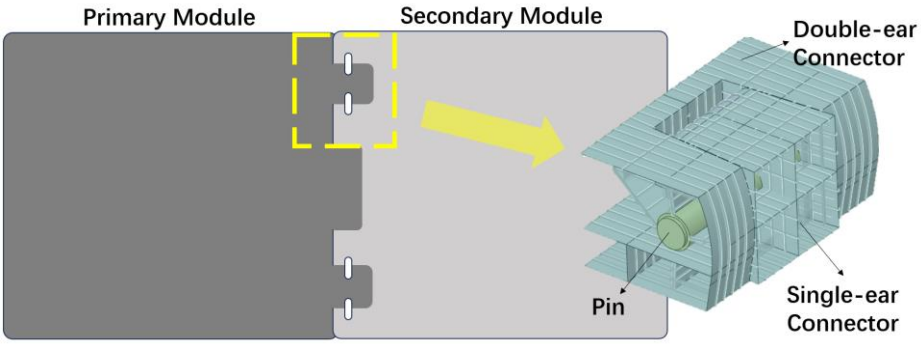

Fig.2. Schematic diagram of the offshore platform

As shown in Fig. 3, the single-ear connector is a semi-symmetric structure with outer and intermediate bulkheads, the latter featuring three access hatches and five

lightening holes. Its parameters, along with those of a single module, are in Table 1.

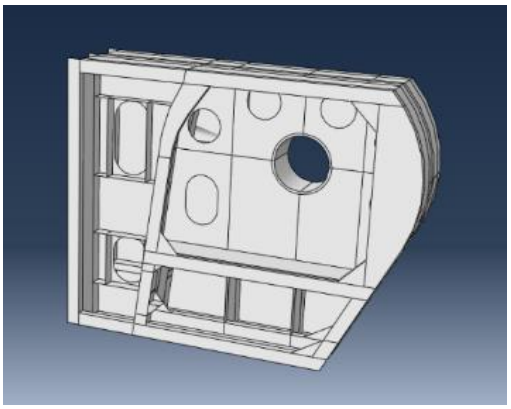

Fig.3. Inner structure of the single-ear connector

Tab.1

Parameters of the offshore platform

Parameters of a single module		Parameters of the single-ear connector	
Length	30.0m	Length	3950.0mm
Width	25.0m	Width	1700.0mm
Height	14.2m	Height	3200.0mm
Displacement	1827.0t	Outer diameter of pins	320.0mm

2.2 Hydroelastic Analysis

Considering potential sea conditions, THAFTS software (version 2.0) calculated the platform's Response Amplitude Operator (RAO) and short-term extreme load profiles to assess the pin's shear force.

The shear force direction primarily aligns with the resultant of F_x and F_z. However, bending from M_x and M_z may cause minor deviations. Under calculated conditions, shear forces can occur at any angle from 0° to 360°, with the peak value being 2679 kN at 13.3° [1,19].

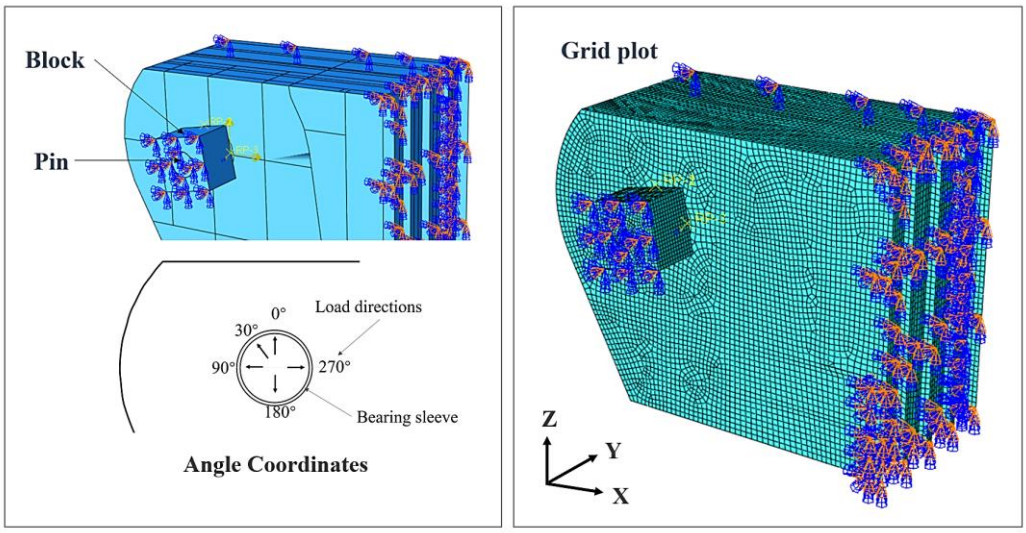

Fig. 4. Details of the connector's simulation analysis

2.3 Finite Element Model

A Finite Element model was built in ABAQUS (2020), as shown in Fig.4. It used 4-node shell elements for the connector, totaling 30,858 elements, and 8-node solid elements for the pin and sleeve. Tab. 2 contains the parameters of the model.

The pin and the connector are tightly assembled through a bearing sleeve, which is integrally welded to the connector structure. For Finite Element Analysis, a loading block is used to simulate the shear force from the adjacent connector.

Tab. 2

Parameters of the Finite Element Models

Elastic Modulus (N/mm^2)		Poisson's Ratio		Mesh Size （mm）		Yield Strength (MPa)	
Connector	Pin Shaft	Connector	Pin Shaft	Connector	Pin Shaft	Connector	Pin Shaft
2.05×10^5	2.05×10^5	0.27	0.27	50	25	355	450

2.4 Constraints Setting

The connector is fixed at its boundaries, with no displacement in the X and Y directions, allowing the block and pin to move freely in the load direction.

A Tie constraint connects the bearing sleeve to the connector. The interaction between the pin and bearing sleeve is modeled using penalty function methods, ensuring rigid contact normally and slight sliding tangentially. The simulation applies Coulomb friction theory with a friction coefficient of 0.1 and initiates with a 0.5mm circumferential gap between the pin and bearing sleeve.

The pin's cross-section and bearing sleeve's outer surface nodes are fixed. Using the MPC (Multi-Point Constraint) method, the sleeve's other outer surface nodes are coupled to a central reference point, restricting rotational movement. A quasi-static nonlinear simulation is conducted using the arc-length method.

3 Feature Elements Selection Based on the Correlation Analysis

3.1 Shear Force Inversion Based on Feature Elements

Assuming the connector is a homogeneous, crack-free elastic object, it is discretized into finite elements. According to Newton's third law, forces between adjacent elements are in equilibrium. The total tension on these elements' surfaces equates to the external load on the object. Consequently, the shear force on the pin can be calculated by summing the tensions in each finite element. This is mathematically represented as follows:

$$\vec{F} = \sum_{i=1}^{n} \overrightarrow{f_i} = \sum_{i=1}^{n} f_i(\delta_{i1} f_{ix}, \delta_{i2} f_{iy}) \tag{1}$$

In Equation (1), $\vec{F}$ represents the shear force vector on the connector's contact surface, indicating the shear force's magnitude and direction. $\overrightarrow{f_i}$ represents the tension vector on finite elements indexed by i (where $i = 1,2 \ldots, n$, and n is the number of finite elements). The x-axis (f_{ix}) and y-axis (f_{iy}) correspond to projection coefficients δ_{i1} and δ_{i2} , respectively, both of which are constants.

The values of f_{ix} and f_{iy} can be calculated based on the σ_{ix}, σ_{iy} and τ_{ixy} in the

corresponding finite element.

$$\vec{F} = \sum_{i=1}^{n} f_i(\sigma_{ix}, \sigma_{iy}, \tau_{ixy}) = \sum_{i=1}^{k} \delta_i f_i(\sigma_{ix}, \sigma_{iy}, \tau_{ixy}) \quad (2)$$

To address the impracticality of measuring stress in each finite element, an optimized approach compresses the entire FE model into "k" feature elements, which significantly reduces the number of required sensors. By measuring feature elements, stress values for each element can be inferred.

3.2 Correlation Analysis Among the Finite Element

The connector is discretized into "m" finite elements (e_i), with the entire set of elements represented as S. The structural response matrix X is obtained through n load steps.

$$\boldsymbol{X} = [\boldsymbol{x_1}\ \boldsymbol{x_2}\ \boldsymbol{x_3} \dots \boldsymbol{x_i} \dots \boldsymbol{x_m}] = \begin{bmatrix} x_1(1) & x_2(1) & \dots & x_i(1) & \dots & x_m(1) \\ x_1(2) & x_2(2) & \dots & x_i(2) & \dots & x_m(2) \\ \vdots & \vdots & \ddots & \vdots & \vdots & \vdots \\ x_1(k) & x_2(k) & \dots & x_i(k) & \dots & x_m(k) \\ \vdots & \vdots & \vdots & \vdots & \ddots & \vdots \\ x_1(n) & x_2(n) & \dots & x_i(n) & \dots & x_m(n) \end{bmatrix} \quad (3)$$

In Equation (3), the stress value of the Finite Element indexed as i with n load steps is represented as $x_i(n)$.

$$\boldsymbol{x_i} = [\boldsymbol{x_i(1)}\ \boldsymbol{x_i(2)} \dots \boldsymbol{x_i(n)}] \quad (4)$$

where i =1,2,…,m.

Correlation analysis assesses the quantitative relationship between variables to ascertain their association. The covariance Cov(x_i,x_j) is used to analyze the similarity in response between any two finite elements, e_i and e_j, under identical load steps.

$$\mathrm{Cov}(x_i,x_j)=E(x_ix_j)-E(x_i)E(x_j) \quad (5)$$

In Equation (5), $E[x_i]$ and $E[x_j]$ represent the expected values of the two variables x_i and x_j, respectively. Due to the different dimensions of the variables, their covariances may exhibit significant numerical variations. To address this, a dimensionless method, the Pearson correlation coefficient (Equation 6), is used for calculation.

$$P_{i,j} = \frac{cov(x_i,x_j)}{Var_i Var_j} \quad (6)$$

$$\begin{aligned} cov(x_i, x_j) &= E(x_i - \overline{x_i})(x_j - \overline{x_j}) \\ &= \frac{1}{n-1}\sum_{k=1}^{n}(x_i(k) - \overline{x_i})(x_j(k) - \overline{x_j}) \\ Var_i &= \frac{1}{n-1}\sum_{k=1}^{n}(x_i(k) - \overline{x_i})^2 \\ Var_j &= \frac{1}{n-1}\sum_{k=1}^{n}(x_j(k) - \overline{x_j})^2 \end{aligned} \quad (7)$$

In Equation (7), Var_i represents the variance of $x_i(n)$, Var_j represents the variance of $x_j(n)$, $\overline{x_i}$ is the mean response value of $x_i(n)$, and $\overline{x_j}$ is the mean response value of $x_j(n)$. The correlation matrix P between any two finite elements is given as Equation (8).

$$\boldsymbol{P} = [\boldsymbol{P_{ij}}]_{\boldsymbol{m\times m}} = \begin{bmatrix} p_{11} & p_{12} & \cdots & p_{1j} & \cdots & p_{1m} \\ p_{21} & p_{22} & \cdots & p_{2j} & \cdots & p_{2m} \\ \vdots & \vdots & \ddots & \vdots & \vdots & \vdots \\ p_{i1} & p_{i2} & \cdots & p_{ij} & \cdots & p_{im} \\ \vdots & \vdots & \vdots & \vdots & \ddots & \vdots \\ p_{m1} & p_{m2} & \cdots & p_{mj} & \cdots & p_{mm} \end{bmatrix} \tag{8}$$

The Correlation coefficient p_{ij}, ranging from -1 to 1, indicates the strength of correlations; a value near zero suggests a weak correlation. This paper concentrates on cases where $p_{ij} > 0.95$, denoting a strong correlation between x_i and x_j in load feedback. Elements with such notable correlations are grouped into clusters, denoted as T.

$$\boldsymbol{S} = \{\boldsymbol{T_1}\ \boldsymbol{T_2}\ \ldots \boldsymbol{T_i}\ \ldots \boldsymbol{T_k}\} \tag{9}$$

In Equation (9), the index i varies from 1 to k. Feature elements (v_i) are selected from each cluster T_i to form a new set, $V = \{v_1, v_2, \ldots, v_i, \ldots, v_k\}$, sensitive to both the magnitude and direction of the shear force.

Using this method, 50 feature elements were identified from a total of 30,858 finite elements, as shown in Fig. 5, which means the structure can be categorized into 50 clusters.

Index of all feature elements:

26,254	28,090	25,753	26,299	5260	27,672	27,910	26,234	25,799	5247
27,158	26,528	27,597	27,645	22,865	26,498	27,943	26,009	27,844	27,572
27,662	25,834	27,765	27,988	26,084	27,738	27,754	25,507	27,241	26,465
28,120	26,631	26,336	26,425	26,346	27,174	27,728	25,888	26,436	25,964
26,049	25,920	26,965	27,425	26,614	22,855	25,980	930	26,316	28,032

Fig. 5. Feature elements identified from a total of 30,858 elements

3.3 Nonlinear Analysis of Simulated Sample Data

Adjacent conditions may exhibit linear relationships under subtle load fluctuations, leading to fewer effective samples and potential distortion of neural network performance. To investigate this, six feature elements (as shown in Fig. 6) and four different angles were randomly selected to analyze their "load-stress" curves (as shown in Fig. 7).

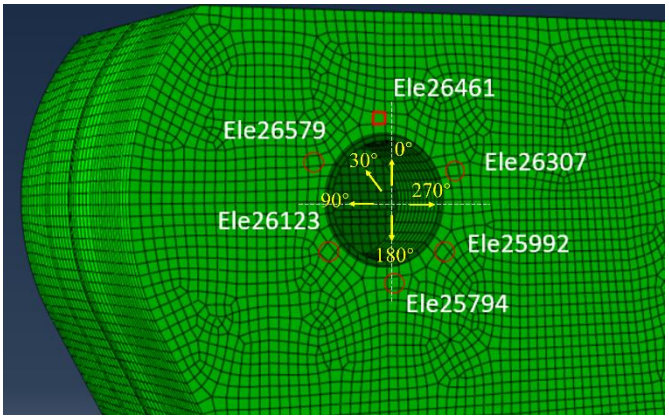

Fig.6. Positions of the six feature elements and the schematic of the load directions

When the angle is rotated from 0° to 20°, adjacent angles show similar magnitudes, as illustrated in Figure 12. However, the combination of feature elements results in a non-linear data pattern. Notably, the input variable for the ANN is the von Mises stress, derived from three variables. Therefore, the input dimension of the ANN is triple the number of feature elements, resulting in increased nonlinearity in samples under adjacent conditions. This ensures that the sample data obtained from simulations are suitable for developing an ANN.

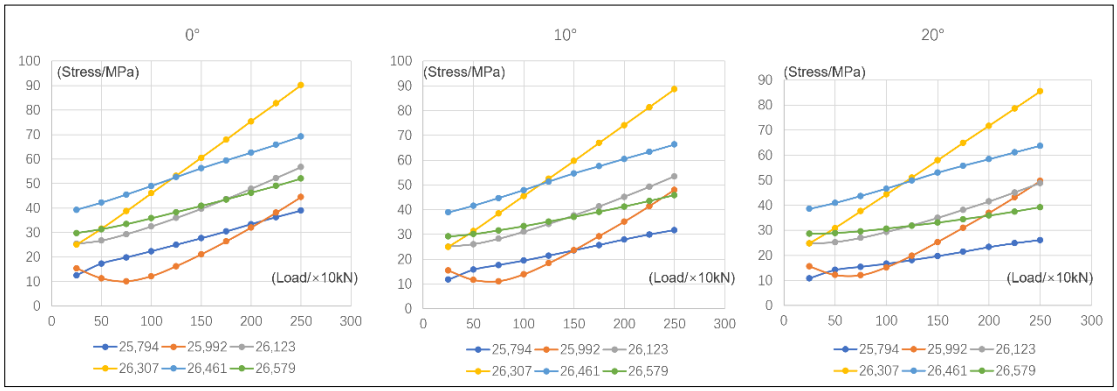

Fig. 7. Linearity of the 6 feature elements at angles of 0°, 10°, 20°

4 Architecture of ANN for Shear Force Inversion

4.1 Data for Developing the ANN

The data for developing an ANN for shear inversion is derived from simulations detailed in Section 2. It comprises 3600 simulated scenarios, where the direction of the shear force varies between 0° and 350° in increments of 10°, and the magnitude of the shear force ranges from 50 kN to 5000 kN, increasing in steps of 50 kN.

The dataset is randomly divided into three disjoint sets: the training set (S_l), the validation set (S_v), and the testing set (S_t).

$$S = \{S_l, S_v, S_t\} \tag{10}$$

Among them, S_l , contains 2400 samples and is used to train the network. S_v , contains 600 samples and is used to evaluate the convergence of the network and decide when to end the training. S_t, contains 600 samples and is used to quantify the network's accuracy in shear force inversion.

4.2 Measurement Positioning

The 50 feature elements are sorted based on stress amplitude, and the count of correlated elements for each is recorded (Fig. 7). Results show that the total count of elements associated with the 50 feature elements is 220,905, significantly exceeding the entire count of finite elements (30,858). This indicates multiple overlaps among the clusters, allowing for the use of fewer feature elements to inverse for the shear force.

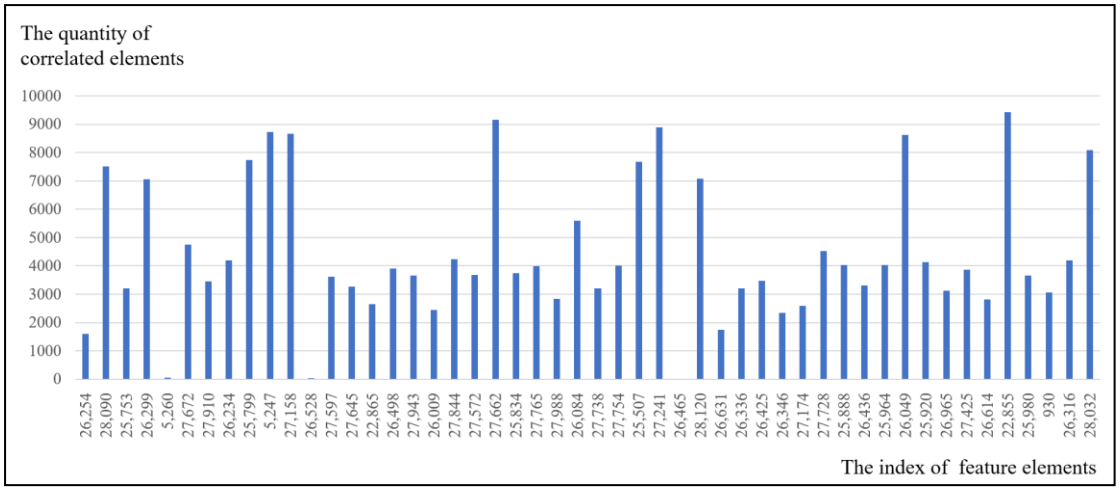

Fig.8. The quantity of correlated elements of each feature element (Load sensitivity from strong to weak)

Fig. 9 illustrates how the number of feature elements (5, 10, 15, 20) affects ANN accuracy. Initially, accuracy increases with more elements, reaching a plateau at 10 and stabilizing at 15. This indicates the first 15 elements are highly correlated with the majority of the entire elements. Therefore, selecting the first 15 feature elements as measurement points, while balancing the challenges and costs, can yield satisfactory inversion accuracy.

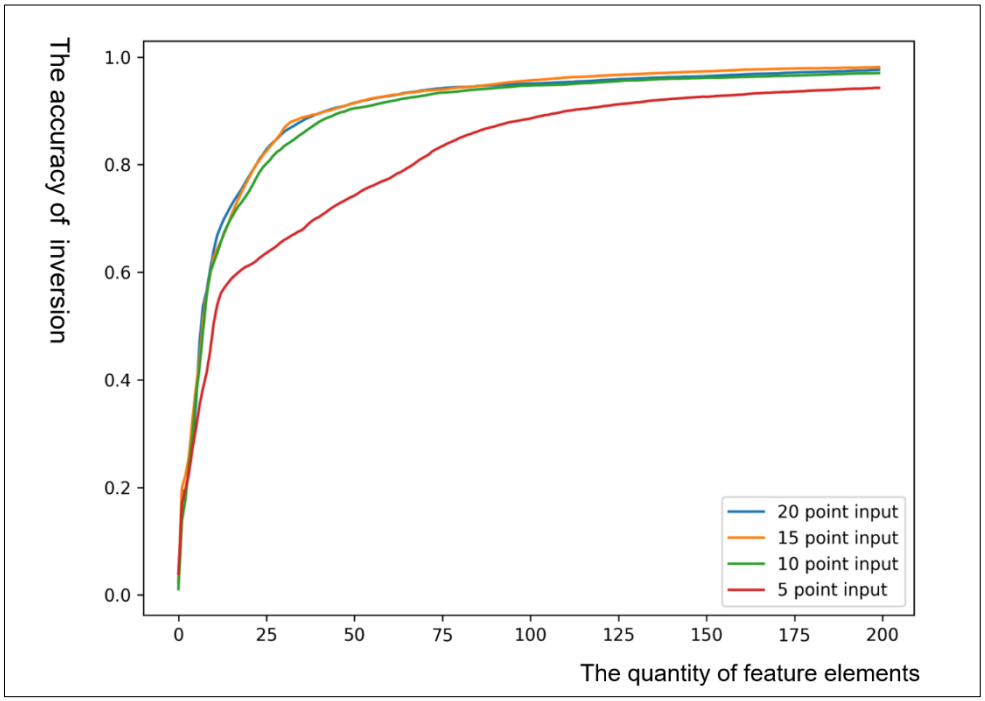

Fig. 9. Impact of the quantity of feature elements on the inversion accuracy

4.3 Convergence Rule Setting

The ANN convergence analysis, without an upper limit on training iterations, is depicted with the x-axis showing training rounds and the y-axis accuracy. The blue curve represents validation set accuracy every 200 epochs, and the red curve shows test set accuracy.

Fig. 10 shows that increased epochs initially boost predictive accuracy, suggesting

underfitting, then reach a plateau indicating stability. However, accuracy later diminishes with more epochs, signifying overfitting. Thus, the ANN's convergence criterion is established: training stops and the model is finalized if validation accuracy decreases by over 5% from the previous epoch.

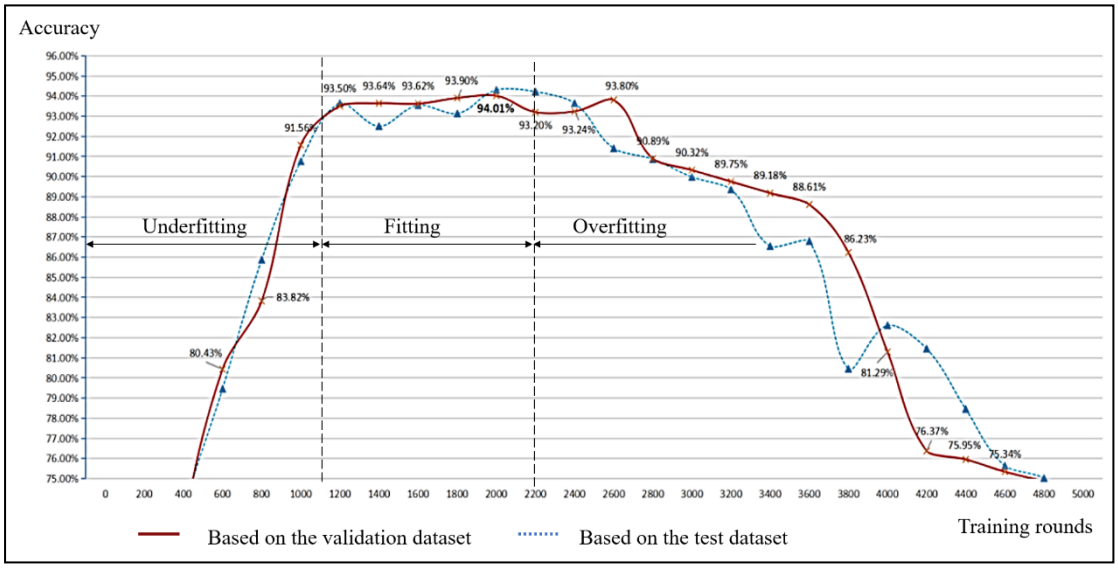

Fig.10. Accuracy curve during the training process

4.4 Generalization Tested by Simulated Conditions

The ANN's generalization performance was assessed with dataset (S_t), using Mean Squared Error (MSE) and Mean Absolute Error (MAE) to analyze shear force inversion accuracy, conducted at intervals of 10°.

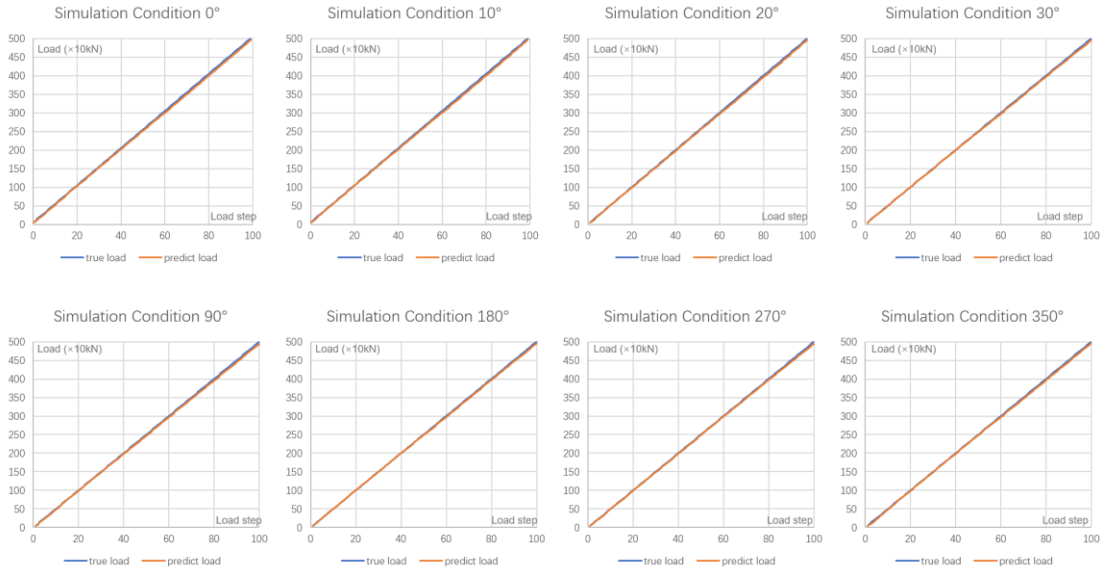

Fig.11. Comparison curves between inverted and theoretical shear force

(1) Fig. 11 shows a comparative curve of shear amplitude inversion using ANN under various conditions. Tab. 3 details the ANN's MAE and MSE for shear inversion at angles ranging from 0 to 5000 kN. The maximum inversion error by the ANN is 1%, along with low MSE values, highlighting its ability to replicate shear magnitudes accurately across different angles.

(2) Tab. 4 compares true shear angles with those inferred. Although the ANN

effectively identifies the range of shear occurrence, it exhibits a significant deviation of 7° between angles of 250° and 320°. Fig. 12 depicts ANN-inferred angle MSE across 36 angles, revealing elevated MSE at 0°, 30°, 90°, 260°, and 300°, indicating inference instability in these scenarios.

Tab. 3

MAE and MSE of shear inversion

Angle (°)	MAE （×10kN）	MSE （×100kN^2）	Angle (°)	MAE （×10kN）	MSE （×100kN^2）
0	5.31	0.33	180	4.95	0.49
10	5.26	0.41	190	4.87	0.41
20	4.80	0.46	200	2.61	0.26
30	4.23	0.55	210	2.89	0.50
40	5.46	0.45	220	3.71	0.36
50	5.60	0.56	230	4.05	0.39
60	4.60	0.41	240	5.02	0.32
70	4.45	0.53	250	4.07	0.31
80	5.80	0.52	260	5.46	0.27
90	5.50	0.41	270	5.57	0.41
100	5.59	0.49	280	4.93	0.42
110	5.72	0.50	290	5.03	0.33
120	3.32	0.45	300	5.87	0.49
130	4.52	0.51	310	4.96	0.38
140	3.89	0.50	320	5.46	0.28
150	4.08	0.56	330	5.25	0.24
160	3.19	0.67	340	5.24	0.26
170	3.21	0.31	350	4.06	0.39

Tab. 4

MAE and MSE of shear inversion

NO.	True angle (°)	Inverted angle (°)	NO.	True angle (°)	Inverted angle (°)
1	0	4.1	19	180	182.1
2	10	11.3	20	190	192.2
3	20	21.8	21	200	201.2
4	30	32.1	22	210	211.2
5	40	41.8	23	220	222.0
6	50	51.9	24	230	232.6
7	60	62.9	25	240	242.2
8	70	73.0	26	250	255.8
9	80	83.7	27	260	267.5
10	90	93.8	28	270	276.5
11	100	102.6	29	280	284.3
12	110	112.2	30	290	298.3
13	120	122.8	31	300	310.7
14	130	132.8	32	310	317.5
15	140	142.7	33	320	326.5
16	150	152.5	34	330	330.0
17	160	162.6	35	340	340.0
18	170	172.6	36	350	360.0

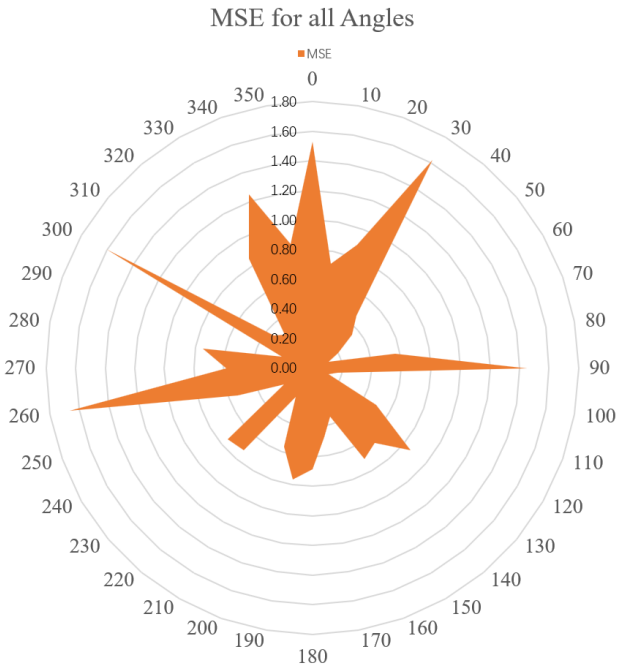

Fig. 12. MSE of the inferred angles

The inconsistency in ANN-inferred angles is due to the limited scope of a simulation dataset containing only 36 values, not adequately covering all angular variations. The ANN's stability in inferring angles will be fine-tuned by incorporating data from physical structures.

5 Fine-tuning of the ANN with Physical Data

The primary importance of fine-tuning lies in minimizing the deviation when transferring an ANN, initially based on simulated data, to real physical structures. This process also enhances the ANN with real measured data, addressing gaps in initial simulations, including the limitations in simulation samples for specific angles as previously mentioned.

5.1 Differences between Simulation Data and Physical Structures

The ANN initially trained on simulation data, requires fine-tuning before deployment for two primary reasons: (1) discrepancies between the simulated model and the physical structure in terms of material properties, boundary conditions, and load simulation; (2) potential geometric errors in the actual measurement location and orientation, compared to the ideal positions in the simulated model.

Figure 13 shows the comparison between ANN-predicted and measured shear force magnitudes upon the ANN's initial deployment on a physical structure at a 10° angle, highlighting significant deviations.

Fig.13. Comparison between Predicted and Measured Value without Fine-tuning

(1) In low-load conditions, the ANN's predictions exhibit random drift due to the absence of distinctive recognition features.

(2) As the load increases from 400 to 1200kN, the ANN's predictions show a step-like pattern, with a deviation of about 600kN from the measured values. This pattern, detailed in Figure 14, demonstrates the ANN's adaptability to identifying load characteristics.

(3) Furthermore, the ANN's predictions fluctuate, initially showing peaks at new load levels and then oscillating around a stable value over extended load durations, exhibiting characteristics of short-term equilibrium and transient volatility.

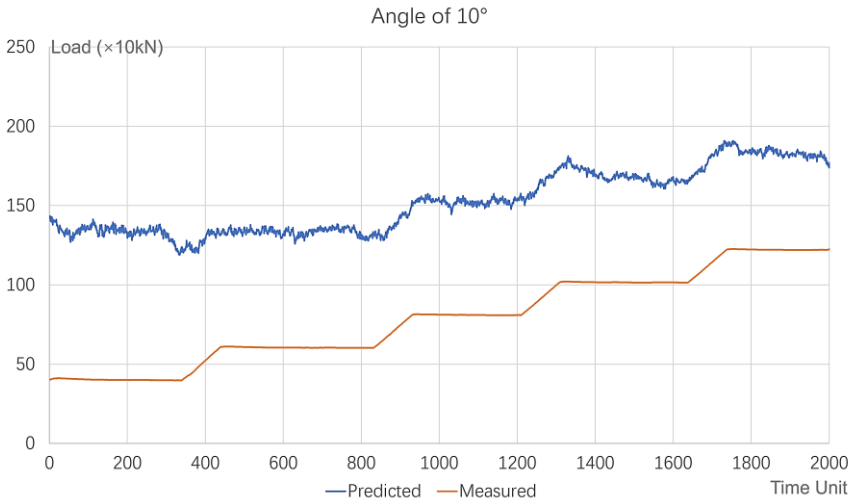

Fig.14. Step-Like Prediction pattern with 600kN deviation in Measured value

5.2 Architecture during Fine-tuning

Figure 13 underscores the necessity of fine-tuning the ANN to enhance its capabilities. Figure 15 shows the fine-tuning process, which involves:

(1) Manual tuning of hyperparameters to improve recognition under low-load conditions.

(2) Addition of an extra layer to the ANN to reduce variations across different load steps. Only these added layers undergo training, using supervised learning with measurement data to fine-tune the output layer parameters via the BP algorithm.

(3) Performing a smoothing operation on the sensors data, using the Savitzky-

Golay filter (with a window length of 41 and a polyorder of 3), to reduce the ANN's sensitivity to transient volatility.

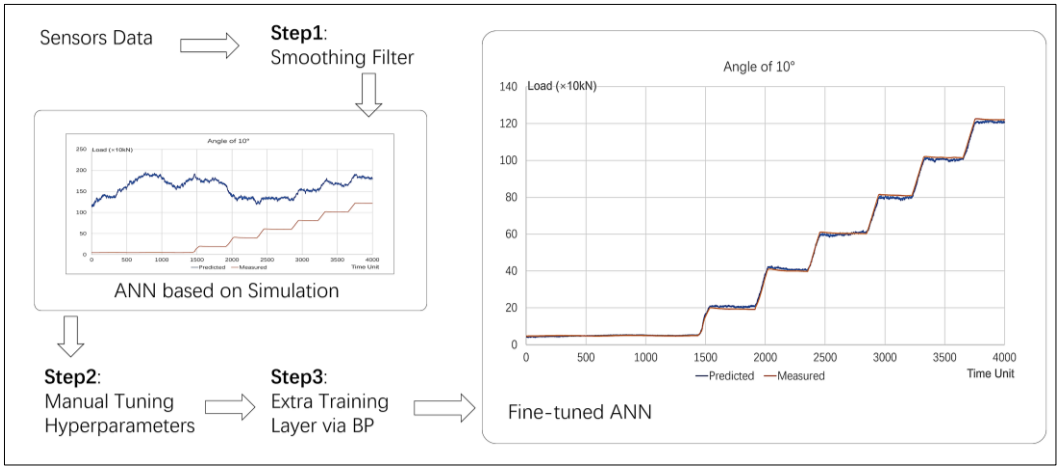

Fig. 15. Fine-tuning Process

6 Accuracy Assessment Based on Physical Structure

6.1 Test Object

The experiment involved a 1:1 connector model to confirm the accuracy of the ANN's shear force predictions [21]. Due to the symmetry in geometry, load, and boundaries in the double-ear connector structure adjacent to the single-ear connector, a solid loading block is used to simulate the adjacent connectors. The shaft sleeve, being a part of the loading block, is tightly fitted with the pin, simulating the interconnection between the connectors. The experiment applies loads to the center of the shaft sleeve using a hydraulic cylinder. Precise control of the shear force is achieved using a force sensor, and the inclined angle is simulated by fixing a bottom block to the cylinder, as illustrated in Fig. 16.

Simulating real constraints, the single-ear connector is fixed on a vertical rigid frame, with axial pin displacement limited at its lateral edges, allowing radial sliding along the pin.

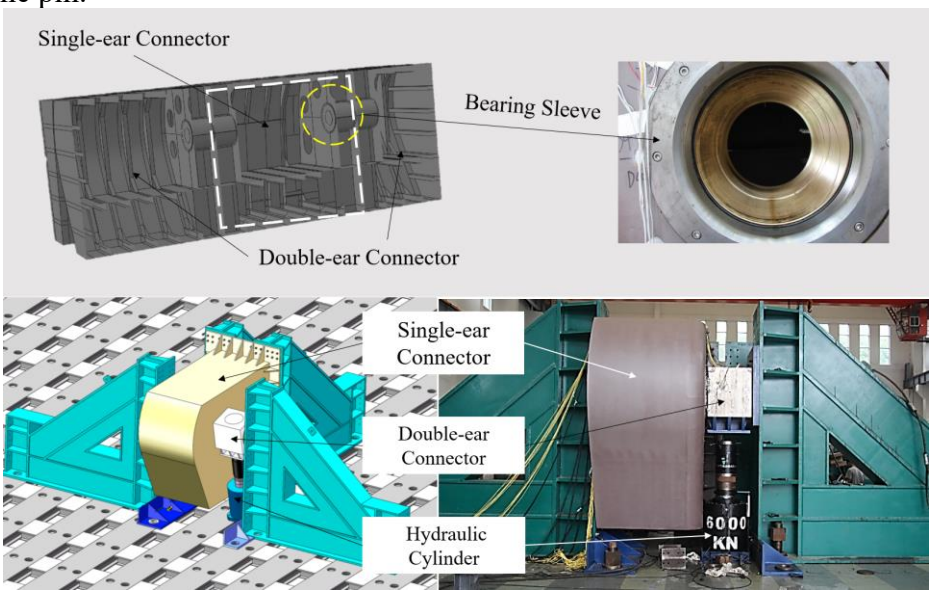

Fig. 16. The framework of the test

6.2 Arrangement of the Sensors

Following the analysis in Section 4.2, 15 stress measurement points were strategically positioned on selected feature elements, as depicted in Fig. 17. Strain gauges and sensors, operating at a frequency of 10 Hz, were used to measure three-dimensional strain.

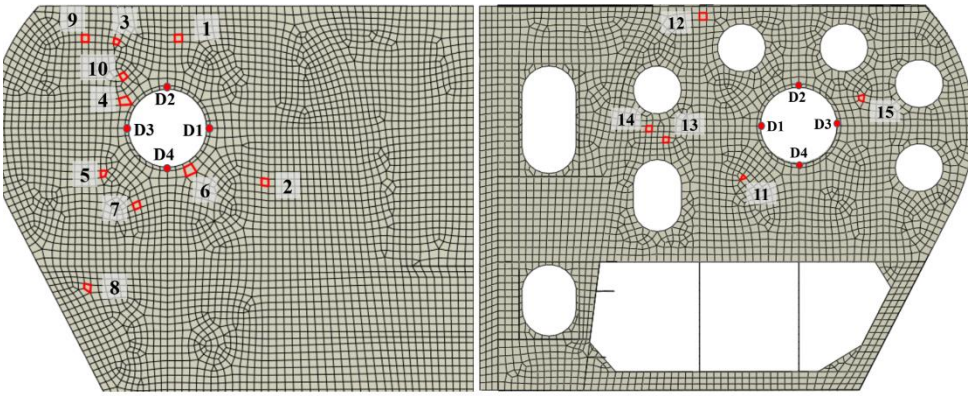

Fig. 17. Sensors' location during the test

6.3 Loading process

The test was conducted within the elastic limits, with the loading scheme detailed in Tab.5. It encompassed various inclinations (shown as Fig.18) at 0°, 10°, 20°, 340°, and 350°. It also included tests at non-integer angles of 13.3° and 346.7° to evaluate the accuracy of an ANN trained solely on measurement data, excluding simulation data during training.

Tab. 5

Detailed loading conditions

Angle	Fine-tuning Loading Scheme (kN)			Validation Loading Scheme (kN)		
	Min Load	Max Load	Load Step	Min Load	Max Load	Load Step
0°	200	1200	100	200	1800	200
10°	200	1200	100	200	1800	200
13.3°	200	1200	100	200	1800	200
20°	200	1200	100	200	1800	200
30°	200	1200	100	200	2000	200
330°	200	1200	100	200	2000	200
340°	200	1200	100	200	1800	200
346.7°	200	1200	100	200	1800	200
350°	200	1200	100	200	1800	200

Notably, to evaluate the ANN's generalization ability, the validation phase employs a broader load range than the fine-tuning phase, ensuring the presence of data not previously encountered by the ANN.

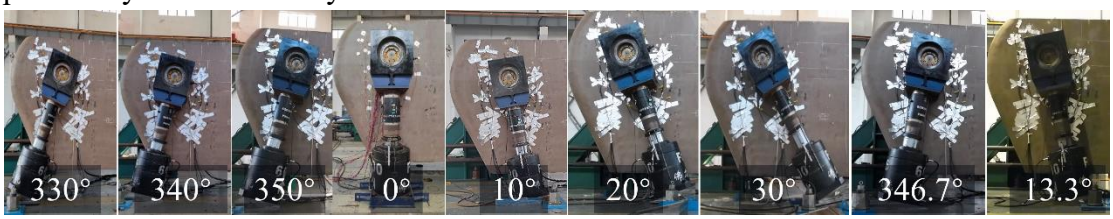

Fig. 18. Unconstrained to illustrate the different loading angles

6.4 Test Results

(1) Fig.19 shows comparison curves between measured and inverted values of shear force for six angles (10°, 20°, 30°, 330°, 340°, and 350°). Tab.6 lists the MAE between the inverted and measured shear force values across the entire loading range for above angles. The results indicate that the shear amplitude curves predicted by the ANN closely match the measured amplitude curves under various conditions, with maximum deviations within 2.7% of the full scale.

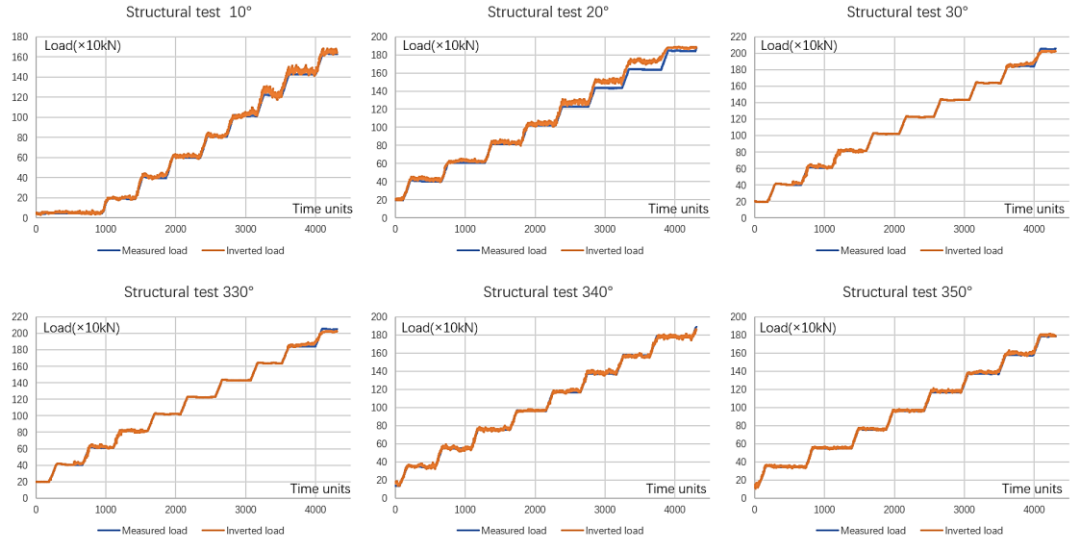

Fig. 19. Comparison curves of measured and inverted shear force

Tab. 6

The MAE between the inverted and measured shear force values

Angle (°)	MAE from Test (×10kN)
10°	5.07
20°	4.24
13.3°	5.75
30°	3.48
330°	1.99
340°	4.50
346.7°	2.53
350°	5.07

(2) Fig.20 shows comparison curves between measured and inverted values of angles, Fig.21 present a radar chart comparing the MSE of angle inversion before and after fine-tuning for the six conditions. After Fine-tuning, the ANN's angle prediction error is reduced to within 2°, demonstrating improved and more stable performance.

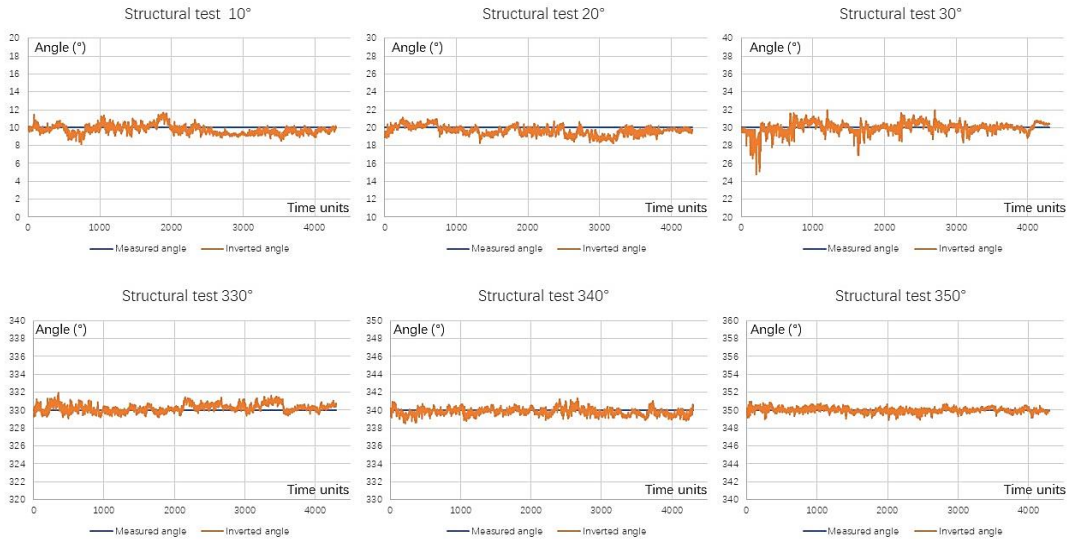

Fig. 20. Comparison curves of measured and inverted angles

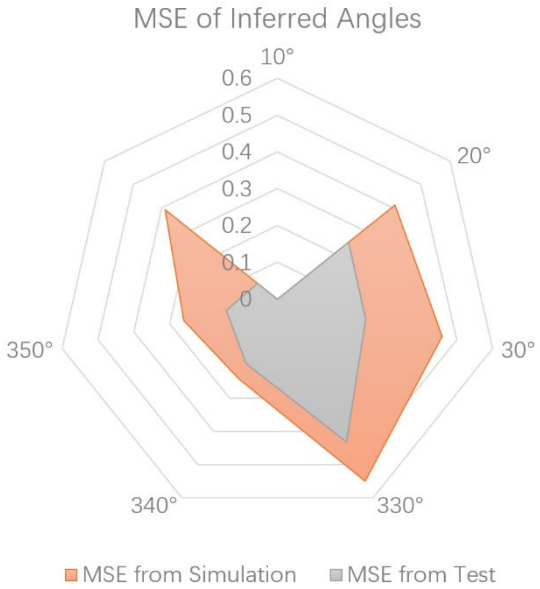

Fig. 21. Comparison of MSE of angle before and after Fine-tuning

(3) Figure 22 shows the comparison curves at angles of 13.3° and 346.7°, demonstrating that the ANN's shear force amplitude predictions closely matched measurements during the loading process, yielding MAEs of 3.2% and 1.4%, respectively, while maintaining angle prediction errors within a 1° margin.

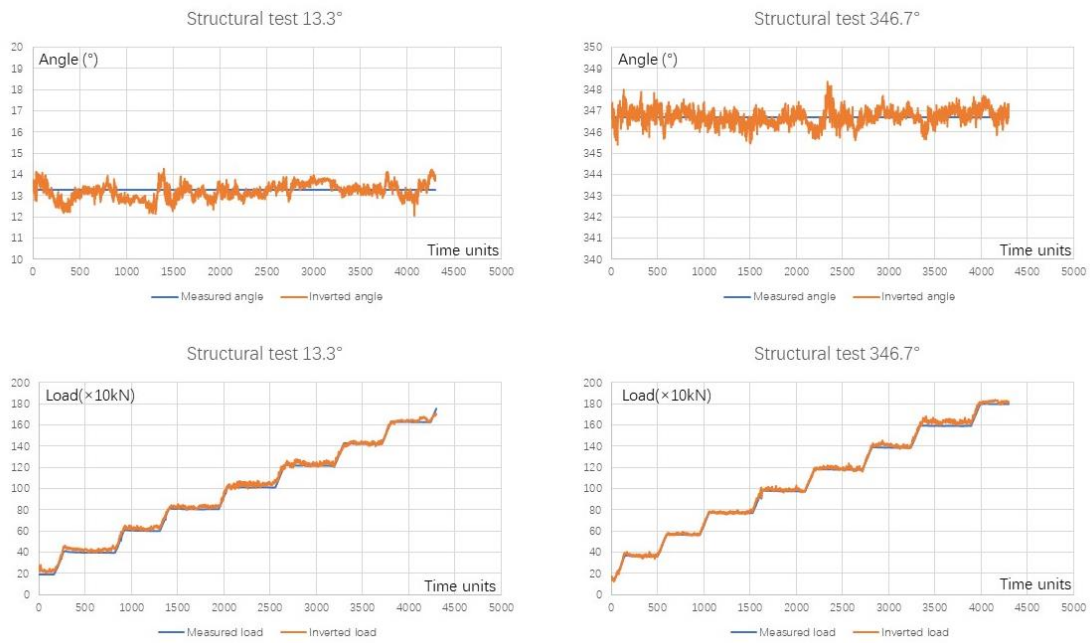

Fig. 22. Comparison between measured and inverted values at 13.3° and 346.7°

6.5 Discussion

(1) Challenges faced by ANN's stability

As the load exceeded 1200 kN, the shear amplitude curve displayed slight oscillations at 10°, with minor deviations at 20°. This can be primarily attributed to two factors:

a) Limited learning range of the ANN

The ANN was not trained and fine-tuned with data beyond 1200 kN, leading to predictions that align with measured values up to this point but become less stable at higher loads. This limitation in the training range of the ANN highlights the need for incorporating a broader spectrum of data for more robust model training.

b) Non-linearity of the input layer

The hydraulic cylinder's load fluctuations were precisely controlled below 0.1%, indicating that the observed slight oscillations above 1200 kN originated from the ANN. A possible explanation is that the transient volatility of the sensors was amplified by a 45-dimensional vector from 15 triaxial stress sensors.

(2) Enhancing the ANN's performance by monitoring data

Retuning the ANN with data obtained beyond 1200 kN, Figure 23 shows that the oscillations between inverted values and actual measurements are eliminated. This suggests that fine-tuning the ANN with a more diverse range of samples from physical structures could further improve the ANN's prediction stability. Future work should concentrate on integrating more monitoring data to refine the ANN's accuracy and stability.

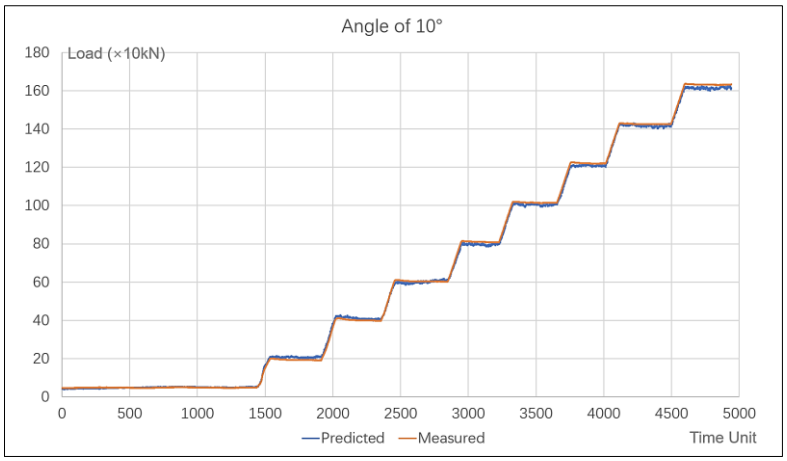

Fig.23. Comparison Curve after retuning with data beyond 1200 kN

7 Conclusions

An inversion method that links sensitive finite elements to the shear force in Offshore Platform Connectors is established through Finite Element simulation and ANN application， which is further augmented by fine-tuning the ANN with measurements from the physical structure, yielding the following insights:

(1) By correlational analysis among 30,858 finite elements, 15 feature elements were identified to develop an ANN for shear force inversion, yielding a maximum shear amplitude error of 1% under diverse load conditions, but resulting in a significant 7° deviation in angle inversion.

(2) Significant deviations were observed when initially transferring an ANN, built on simulated data, to real-world structures. The fine-tuning process notably reduced these deviations, lowering amplitude prediction errors to below 2.7% and improving angle accuracy from a deviation of 7° to less than 2°. Particularly at specific angles, such as 13.3° and 346.7°, the ANN consistently yielded reliable results, emphasizing the effectiveness of fine-tuning in enhancing accuracy with real measurement data.

(3) The accumulation of monitoring data enables definitive improvement in the ANN's prediction stability, achieved by fine-tuning with a broader range of samples from physical structures.

In future research, it is important to consider that a single sensor’s malfunction can impact the ANN's robustness. The next step is to explore Transformer models, which could remain stable even with partial sensor failure, due to their inherent attention mechanisms.

Acknowledgements

This research was funded by National Key Research and Development Program of China (NO. 2021YFC2802300); China State Scholarship Fund (No. 202208320260).

References

[1] Wu Y, Ding J, Gu X, et al. The progress in the verification of key technologies for floating structures near islands and reefs[J]. Journal of Hydrodynamics, 2021, 33: 1-12.

[2] Bartlett F D, Flannelly W G. Model verification of force determination for measuring vibratory loads[J]. Journal of the American Helicopter Society, 1979, 24(2): 10-18.

[3] Blakeborough A, Clément D, Williams M S, et al. Novel load cell for measuring axial force, shear force, and bending movement in large-scale structural experiments[J]. Experimental mechanics, 2002, 42: 115-122.

[4] Zweiri Y H, Whidbourne J F, Seneviratne L D. Numerical inversion of the dynamic model of a single-cylinder diesel engine[J]. Communications in numerical methods in engineering, 2000, 16(7): 505-517.

[5] Wu X, Argus D F, Heflin M B, et al. Site distribution and aliasing effects in the inversion for load coefficients and geocenter motion from GPS data[J]. Geophysical research letters, 2002, 29(24): 63-1-63-4.

[6] Wang Q, Yu P, Chang X, et al. Research on the bow-flared slamming load identification method of a large container ship[J]. Ocean Engineering, 2022, 266: 113142.

[7] Ikonen T, Peltokorpi O, Karhunen J. Inverse ice-induced moment determination on the propeller of an ice-going vessel[J]. Cold Regions Science and Technology, 2015, 112: 1-13.

[8] Vuorio J, Riska K, Varsta P. Long term measurements of ice pressure and ice induced stresses on the icebreaker sisu in winter 1978[R]. 1979.

[9] Desanghere G. Indirect identification of excitation forces by modal coordinate transformation[C]//Proc. 3rd Int. Modal Analysis Conference. 1985: 685-690.

[10] O'Callahan J, Piergentili F. Force estimation using operational data[C]//Proceedings of the 14th international modal analysis conference. 1996, 2768: 1586.

[11] Ramazani M R, Noroozi S, Koohgilani M, et al. Determination of the static pressure loads on a marine composite panel from strain measurements utilising artificial neural networks[J]. Proceedings of the Institution of Mechanical Engineers, Part M: Journal of Engineering for the Maritime Environment, 2013, 227(1): 12-21.

[12] He Z C, Lin X Y, Li E. A novel method for load bounds identification for uncertain structures in frequency domain[J]. International Journal of Computational Methods, 2018, 15(06): 1850051.

[13] Ren H, Feng G, Liu H, et al. Dynamic Load Inversion Method of Ship Body Based on Influence Coefficient Matrix[C]//International Conference on Offshore Mechanics and Arctic Engineering. American Society of Mechanical Engineers, 2019, 58783: V003T02A027.

[14] Si Hai-long, Gu Xue-kang, Hu Jia-jun. Model Experiment Method of Container Ship’s Torsion Moment and Shear Force [J]. Journal of Ship Mechanics,2020,24(12):1657-1667.

[15] Mubarak A A, Sitepu G, Alie M Z M. Kekuatan Batas Lambung Kapal dalam Menahan Momen Lentur Vertikal[J]. Jurnal Penelitian Enjiniring, 2018, 22(1): 56-61.

[16] Sutrisno W, Alrasyid H. Structural Performance Investigation of Ship Lift Hoist Pile Structure Exposed to Tropical Marine Environment[J]. Int. J. Adv. Sci. Eng. Inf. Technol, 2020, 10: 1564-1570.

[17] Cooper S B, DiMaio D. Static load estimation using artificial neural network: Application on a wing rib[J]. Advances in Engineering Software, 2018, 125: 113-125.

[18] Nan M, Hu J, Waang X, et al. Study on Ice Load Inversion Based on LSTM Networks[J]. Journal of Ship Mechanics, 2021, 25(12).

[19] Miao Y, Cheng X, Ding J, et al. Investigation on hydrodynamic performance of a two-module semi-submersible offshore platform[J]. Ships and Offshore Structures, 2022, 17(3): 607-618.

[20] Zhang H C, Xu D L, Lu C, et al. Connection effect on amplitude death stability of multi-module floating airport[J]. Ocean Engineering, 2017, 129: 46-56.

[21] Zhang T, Hu J, Oterkus E, et al. Reconstructing the global stress of marine structures based on Artificial-Intelligence-Generated content[J]. Applied Sciences, 2023, 13(14): 8196.